Near-Field MIMO-ISAR Millimeter-Wave Imaging

Josiah Wayland Smith[1], Muhammet Emin Yanik[2], and Murat Torlak[1]

[1]Dept. of Electrical and Computer Engineering, The University of Texas at Dallas, Richardson, TX, United States
[2]Radar and Analytics, Texas Instruments, Dallas, TX, United States

a 77

Single-Input-Single output (SISO)

three-dimensional (3-D)

cylindrical/SAR

***Abstract*—Multiple-input-multiple output (MIMO) millimeter-wave (mmWave) sensors for synthetic aperture radar (SAR) and inverse SAR (ISAR) address the fundamental challenges of cost-effectiveness and scalability inherent to near-field imaging. In this paper, near-field MIMO-ISAR mmWave imaging systems are investigated and developed. The rotational ISAR (R-ISAR) regime investigated in this paper requires rotating the target at a constant radial distance from the transceiver and scanning the transceiver along a vertical track. Using an GHz mmWave radar, a high resolution 3-D image can be reconstructed from this two-dimensional scanning taking into account the spherical near-field wavefront. While prior work in literature consists of SISO-ISAR algorithms or computationally sluggish MIMO-CSAR image reconstruction algorithms, this paper proposes a novel algorithm for efficient MIMO 3-D holographic imaging and details the design of a MIMO R-ISAR imaging system. The proposed algorithm applies a multistatic-to-monostatic phase compensation to the R-ISAR regime allowing for use of highly efficient ~~single pixel~~ algorithms. We demonstrate the algorithm's performance in real-world imaging scenarios on a custom prototype MIMO R-ISAR platform. Our fully integrated system, consisting of an mechanical scanner and efficient imaging algorithm, is capable of pairing the scanning efficiency of the MIMO regime with the computational efficiency of single pixel image reconstruction algorithms algorithms**

***Index Terms*—millimeter-wave (mmWave), multiple-input multiple-output (MIMO), inverse synthetic aperture radar (SAR), three-dimensional (3-D) imaging.**

ISAR

monostatic

I. Introduction

Over the past several decades, developments in system-on-chip complementary metal oxide semiconductor (CMOS) radio frequency integrated circuits (RFIC) have resulted in the emergence of frequency modulated continuous wave (FMCW) millimeter wave (mmWave) radars as a cost-effective solution for imaging applications. Near-field mmWave 3D imaging systems have been demonstrated effective for a host of applications, including concealed weapon detection [1]–[3], nondestructive testing [4], [5], ground penetrating radar [6]. The 3D holographic imaging regime has been investigated in the rectilinear (planar) mode [7], [8] and in cylindrical mode [9]. Additionally, progress has been made towards efficient algorithms for single-input-single-output (SISO) monostatic array synthetic aperture radar (SAR) [10] and multi-input-multi-output (MIMO) multistatic array SAR [11]. Specifically, Gao's work at China's National University of Defense and Technology (NUDT) has demonstrated algorithms for 2-D circular SAR (CSAR) imaging [12] and 3-D MIMO-CSAR imaging [13]. While SISO-CSAR algorithms proposed by Sheen [14], Laviada [15], Gao, and others are efficient in generating high resolution 3-D holographic images, they ignore the multistatic effects from a MIMO array, resulting in aliasing and phase mismatch from the ideal SISO case. While, MIMO-CSAR algorithms have been developed in attempt to solve such issues, these algorithms are computationally expensive and inefficient in comparison to their SISO counterparts. In this paper, we propose a resolution to this dilemma by leveraging the benefits of MIMO-CSAR, fewer antenna elements and cost efficiency, with the streamlined computational efficiency of the SISO-CSAR algorithms to produce a highly efficient high-resolution 3-D imaging algorithm. Under this MIMO rotation ISAR (R-ISAR) regime, a robust imaging system is prototyped to verify the proposed algorithm and demonstrate its performance.

3-D

3-D

The rest of this paper is formatted as follows. Section II ~~overviews the FMCW signal model~~, the echo signal from the MIMO R-ISAR scenario ~~shown in Fig. 1~~, and the multistatic-to-monostatic conversion. ~~Section III contains the derivation~~ for the 3-D image reconstruction algorithm in the SISO R-ISAR regime and crucial multistatic-to-monostatic phase correction. Section IV proposes a novel efficient 3-D imaging algorithm consisting of key results from Sections II and III. ~~Next~~, Section V overviews issues including sampling criteria and spatial resolution. Section VI verifies the proposed algorithm in simulation. The imaging prototype is described in Section VII. Real 3-D imaging results are reported in Section VIII, followed finally by conclusions.

proposed

II. MIMO R-ISAR Signal Model

A. MIMO Rotational ISAR (R-ISAR) Echo Signal

The MIMO R-ISAR scenario, as shown in Fig. 1, consists of a rotational scanner whose center is the origin and a MIMO array scanned along the y-axis (vertically), and located at a constant distance of R_0 from the center of the rotator. The position of the transmitter and receiver pair from each point in the target domain (x, z, y) depends on the rotation angle θ and the distance R_0.

distance

(x,y,z) is better.

$$R_T = \sqrt{(x - R_0 cos\theta)^2 + (z - R_0 sin\theta)^2 + (y - y'_T)^2},$$
$$R_R = \sqrt{(x - R_0 cos\theta)^2 + (z - R_0 sin\theta)^2 + (y - y'_R)^2}. \quad (1)$$

explain y_T and y_R in a short sentence

I will depict R_0 and θ in the figure.

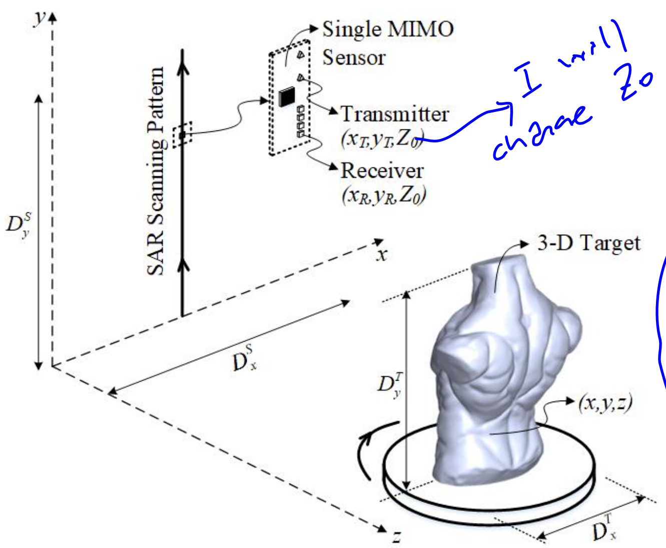

I will change Z_0

Fig. 1: The geometry of the MIMO R-SAR imaging configuration, where a cylindrical aperture is synthesized by mechanically moving a linear MIMO array vertically and rotating the target.

explain θ and k

The MIMO echo signal from the R-ISAR scenario can be modeled as:

lets keep the order as x, y, z

$$s(\theta, k, y'_T, y'_R) = \iiint \frac{p(x,z,y)}{R_T R_R} e^{jk(R_T+R_R)} dxdzdy. \quad (2)$$

B. Multistatic-to-Monostatic Conversion

The received echo data from the multistatic MIMO array ~~undergo~~ undergoes a simple transformation to approximate its counterpart echo signal from the virtual-SISO array elements. To convert this 4-D MIMO signal to a 3-D virtual-SISO signal, the following phase compensation is performed [16], [17],

explain y'

$$\hat{s}(\theta, k, y') = s(\theta, k, y'_T, y'_R) e^{-jk\frac{d_y^2}{4R_0}}. \quad (3)$$

explain d_y

This compensation is a crucial step in the algorithm. By compensating the phase of the multistatic MIMO signal to obtain an approximate of the echo signal from virtual elements located at the midpoint of each MIMO transmitter/receiver pair, this virtual-SISO data can be fed into the efficient 3-D imaging algorithm derived in section III.

III. Derivation of 3-D Image SISO Reconstruction Algorithm

The derivations given in this section are similar to the CSAR algorithm derived by Sheen in [14], but contain several key differences vital performing successful 3-D holographic image reconstruction for a circular scanning scenario.

Using the R-ISAR scenario shown in Fig. 1, the return signal from a monostatic SISO transceiver, neglecting amplitude terms, can be modeled as

$$\hat{s}(\theta, k, y') = \iiint p(x,z,y) e^{j2kR} dxdzdy, \quad (4)$$

where

$$R = \sqrt{(x - R_0 cos\theta)^2 + (z - R_0 sin\theta)^2 + (y - y')^2}, \quad (5)$$

and $p(x,z,y)$ is the complex reflectivity function of the target scene. Using the method of stationary phase (MSP), the exponential term in (4) can be decomposed by ~~(6)~~. Note that an identical result can be found by decomposing the free-space Green's function of a point source in the spatial spectral domain [18], [19].

$$e^{j2k\sqrt{(R_0 cos\theta - x)^2 + (R_0 sin\theta - z)^2 + (y-y')^2}} = \iint e^{jk_r cos\phi(R_0 cos\theta - x) + jk_r sin\phi(R_0 sin\theta - z) + jk_{y'}(y-y')} d\phi dk_{y'}, \quad (6)$$

where the angle of each plane wave component in the $x-z$ plane is $\phi \in [-\pi/2, \pi/2]$, and $k_{y'}$ is the y-component of the wavenumber bounded by $k_{y'} \in [-2k, 2k]$. Using the dispersion relation

$$4k^2 = k_x^2 + k_y^2 + k_z^2, \quad (7)$$

we define k_r as the wavenumber component in the $x-z$ plane as

$$k_r = \sqrt{k_x^2 + k_z^2} = \sqrt{4k^2 - k_y^2}. \quad (8)$$

Combining the above relations yields

$$\hat{s}(\theta, k, y') = \iint \left[\iiint p(x,z,y) e^{-j(k_r cos\phi)x - j(k_r sin\phi)z - jk_{y'}y} dxdydz \right] \times e^{jk_r Rcos(\theta-\phi) + jk_{y'}y'} d\phi dk_{y'}, \quad (9)$$

The term inside the $[\bullet]$ brackets is the ~~three-dimensional~~ 3-D Fourier transform of the reflectivity function. Using the following Fourier transform pair

$$p(x,z,y) \iff P(k_r cos\phi, k_r sin\phi, k_y), \quad (10)$$

(9) yields

$$\hat{s}(\theta, k, y') = \iint e^{jk_r Rcos(\theta-\phi)} P(k_r cos\phi, k_r sin\phi, k_y) e^{jk_{y'}y'} d\phi dk_{y'}. \quad (11)$$

Taking the Fourier transform with respect to y' on both sides and dropping the distinction between z' and z due to coincidence of the domains:

y' y

$$\hat{S}(\theta, k, k_y) = \int_{-\frac{\pi}{2}}^{\frac{\pi}{2}} e^{jk_r Rcos(\theta-\phi)} P(k_r cos\phi, k_y, k_r sin\phi) d\phi. \quad (12)$$

~~Define:~~ Defining

$$\hat{P}(\phi, k_r, k_y) \triangleq P(k_r cos\phi, k_r sin\phi, k_y) \tag{13}$$
$$g(\theta, k_r) \triangleq e^{jk_r R_0 cos\theta}. \tag{14}$$

Now:

$$\hat{S}(\theta, k, k_y) = \int_{-\frac{\pi}{2}}^{\frac{\pi}{2}} g(\theta - \phi, k_r)\hat{P}(\phi, k_r, k_y)d\phi, \tag{15}$$

which represents a convolution in the θ domain:

$$\hat{S}(\theta, k, k_y) = g(\theta, k_r) \circledast_\theta \hat{P}(\theta, k_r, k_y), \tag{16}$$

where $\circledast_\theta$ is the convolution operator along the θ domain.

Taking the Fourier transform across the θ domain on both sides yields:

$$\hat{S}(\Theta, k, k_y) = G(\Theta, k_r)\tilde{P}(\Theta, k_r, k_y), \tag{17}$$

where

$$G(\Theta, k_r) = FT_{1D}^{(\theta)}[g(\theta, k_r)], \tag{18}$$
$$\tilde{P}(\Theta, k_r, k_y) = FT_{1D}^{(\theta)}[\hat{P}(\theta, k_r, k_y)] \tag{19}$$

Solving for $\tilde{P}$ by taking the inverse filter $G^*(\Theta, k_r)$ and then taking an inverse Fourier transform across the Θ domain for both sides to obtain $\hat{P}$:

$$\tilde{P}(\Theta, k_r, k_y) = \hat{S}(\Theta, k, k_y)G^*(\Theta, k_r), \tag{20}$$
$$\hat{P}(\theta, k_r, k_y) = IFT_{1D}^{(\Theta)}\left[\hat{S}(\Theta, k, k_y)G^*(\Theta, k_r)\right] \tag{21}$$

By (13):

$$P(k_r cos\theta, k_r sin\theta, k_y) = IFT_{1D}^{(\Theta)}\left[\hat{S}(\Theta, k, k_y)G^*(\Theta, k_r)\right], \tag{22}$$

where $k_x = k_r cos\theta$ and $k_z = k_r sin\theta$. $\hat{P}$ will be a non-uniformly sampled function of θ and k_r and will need to be interpolated onto a uniform (k_x, k_z, k_y) grid via Stolt interpolation using the equation (19) and the following relations:

$$\theta = tan^{-1}\left(\frac{k_z}{k_x}\right), \tag{23}$$
$$k = \frac{1}{2}\sqrt{k_x^2 + k_y^2 + k_z^2}. \tag{24}$$

The Stolt interpolation process will be denoted by the $\mathcal{S}[\bullet]$ operator, such that:

$$P(k_x, k_z, k_y) = \mathcal{S}[P(k_r cos\theta, k_r sin\theta, k_y)]. \tag{25}$$

Finally, the algorithm can be summarized by (26) and (27).

$$p(x, z, y) = IFT_{3D}^{(k_x, k_z, k_y)}\left[P(k_x, k_z, k_y)\right], \tag{26}$$
$$P(k_x, k_z, k_y) = \mathcal{S}\left[IFT_{1D}^{(\Theta)}\left[FT_{2D}^{(\theta, y)}\left[\hat{s}(\theta, k, y)\right]G^*(\Theta, k_r)\right]\right]. \tag{27}$$

IV. Proposed 3-D Image MIMO Reconstruction Algorithm

Combining the results from Section II and III, the complete multistatic-to-monostatic 3-D image reconstruction algorithm can be written as the following.

Efficient MIMO R-ISAR 3-D Holographic Imaging Algorithm

1) Gather the raw MIMO echo data as $s(\theta, k, y_T, y_R)$.
2) Perform the phase compensation described in (3) to acquire $\hat{s}(\theta, k, y)$.
3) Perform a 2-D FFT across the θ and y dimensions of the phase corrected data to obtain $\hat{S}(\Theta, k, k_y)$.
4) Generate the azimuth filter $g(\theta, k_r) \triangleq e^{jk_r R_0 cos\theta}$ and implement an FFT across the θ dimension to compute the spectral azimuth filter $G(\Theta, k_R)$
5) Multiply $\hat{S}(\Theta, k, k_y)$ by the inverse filter $G^*(\Theta, k, k_y)$ and perform an IFFT across the Θ domain to obtain $P(k_r cos\theta, k_r sin\theta, k_y)$.
6) Apply Stolt interpolation using the relations in (8), (23), and (24) to transform the polar spatial spectral $P(k_r cos\theta, k_r sin\theta, k_y)$ to the Cartesian $P(k_x, k_z, k_y)$.
7) Finally, compute a 3-D IFFT across k_x, k_z, and k_y to recover the complex reflectivity function $p(x, z, y)$.

V. Discussion of Key Imaging Issues

A. Sampling Criteria

Akin to all sampling applications, spatial sampling in the R-ISAR regime must satisfy the spatial Nyquist theorem. Accordingly, the following sampling criteria must be satisfied for alias-free 3-D holographic image reconstruction as discussed in [2], [13], [14], [20].

$$\Delta k < \frac{\pi}{2R_T}, \tag{28}$$
$$\Delta y < \frac{\lambda\sqrt{(D_S + D_T)^2/4 + R_0^2}}{2(D_S + D_T)}, \tag{29}$$
$$\Delta\theta < \frac{\pi\sqrt{R_0^2 + R_T^2}}{2k_{max}R_0R_T}. \tag{30}$$

R_T is the maximum radius of the target scene, D_T is the target height, D_S is the scanning height, and k_{max} is the maximum wavenumber.

B. Spatial Resolution

Another significant point of discussion for SAR imaging systems is spatial resolution. Vertical resolution is independent of the horizontal rotation and can be calculated using the effective aperture approach as shown in [2].

$$\delta_y \approx \frac{\lambda_c R_0}{2D_S} \tag{31}$$

Where λ_c is the wavelength of the center frequency. To derive the radial resolution, the problem is restricted to a 2-D horizontal plane, thereby removing the vertical element of the scan. Along this horizontal plane, the point spread function (PSF) can be computed analytical as [21]:

$$PSF(r,\theta) = k_{max}\frac{J_1(2k_{max}r)}{\pi r} - k_{min}\frac{J_1(2k_{min}r)}{\pi r} \quad (32)$$

From (32), the horizontal resolution can be deduced [22]. $J_1(\bullet)$ represents the first-order Bessel function and k_{max} and k_{min} are the maximum and minimum wavenumbers, respectively.

$$\delta_R = \frac{2.4}{k_{max} + k_{min}} \quad (33)$$

For both the vertical and horizontal resolutions, an ideal point reflector is employed for simplicity sake. However, real-world applications involving real target scenes, this type of idea spatial resolvability is rarely achieved [13]. Accordingly, these expressions serve as a lower limit on the empirical spatial resolution.

VI. R-ISAR SIMULATIONS

To simulate the echo signal, targets are modeled as a point reflectors in the scene. Using equation (34), echo signals are generated via MATLAB scripts.

? we don't need them, just refer (2)

$$s(\theta, k, y'_T, y'_R) = \sum_{i=1}^{N_p} \frac{p(x_i, z_i, y_i)}{R_T R_R} e^{jk(R_T + R_R)} \quad (34)$$

$$R_T = \sqrt{(x_i - R_0 cos\theta)^2 + (z_i - R_0 sin\theta)^2 + (y_i - y'_T)^2},$$
$$R_R = \sqrt{(x_i - R_0 cos\theta)^2 + (z_i - R_0 sin\theta)^2 + (y_i - y'_R)^2}. \quad (35)$$

Where N_p is the number of distinct point scatterers. Parameters used in the simulations are provided in Table I. θ_{max} is the maximum rotation angle, N_y is the number of vertical captures, Δy is the vertical spacing between MIMO captures, and f_c is the center frequency of the FMCW chirp.

TABLE I: MIMO Radar Parameters

R_0	$\Delta\theta$	θ_{max}	N_y	Δy	B	f_c
0.25 m	0.036°	360°	64	2λ	4 GHz	79 GHz

A. PSF

(2)

First, the point spread function (PSF) is simulated by a single point reflector placed off of the rotator's center. The echo signal is simulated by (34) in MATLAB. Then, the image is reconstructed using the proposed algorithm described in Section IV. The 3-D PSF reflectivity function, reconstructed PSF, and slices of the PSF along each dimensional pair are shown in Figure 2

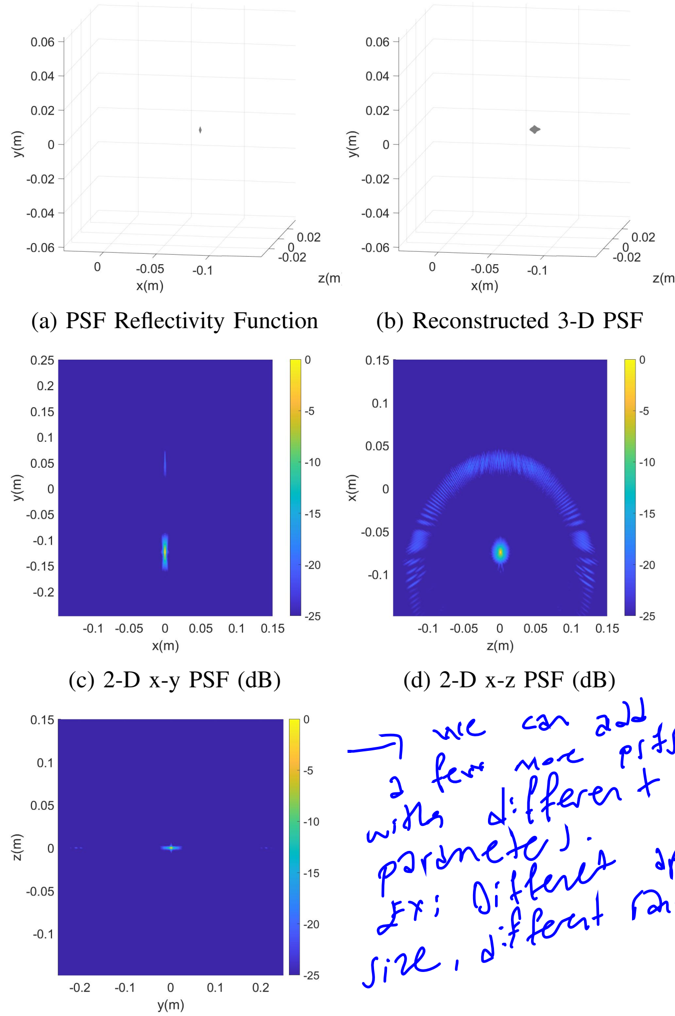

(a) PSF Reflectivity Function (b) Reconstructed 3-D PSF

(c) 2-D x-y PSF (dB) (d) 2-D x-z PSF (dB)

(e) 2-D y-z PSF (dB)

→ we can add a few more psfs with different parameters. Ex: different aperture size, different range, etc

Fig. 2: 3-D input off-center point spread reflectivity function (a), 3-D output reconstructed PSF (b), 2-D vertical vs. cross range PSF (c), 2-D range vs. cross range PSF (d), 2-D range vs. vertical PSF (e)

B. 3D Points

Additionally, to verify the algorithm in simulation, as set of points in a 3-D grid are generated and their echo signal is simulated. The algorithm again effectively reconstructs the images producing a nearly perfect duplicate of the input reflectivity function.

With successful verification of the algorithm in simulation, a custom prototype R-ISAR scanner is built to experimentally capture data and test the algorithm's image quality on real echo data.

VII. EXPERIMENTAL SETUP

A cylindrical aperture is synthesized by mechanically moving a linear MIMO array continuously along a vertical track pattern, and rotating the target as shown in Fig. 1. The

,

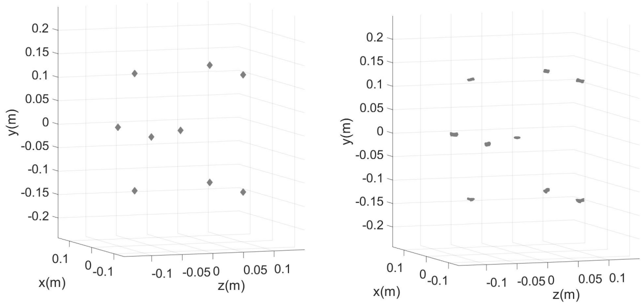

(a) Reflectivity Function (b) Reconstructed Image

Fig. 3: 3-D input grid of points reflectivity function (a), 3-D output reconstructed image (b)

system consists of Texas Instruments (TI) IWR1443-Boost, mmWave-Devpack, and TSW1400 [23] mounted on a 2-D vertical and horizontal scanner as shown in Figure 4a. For this application, only the vertical motion is used. The scanned object is mounted on rotator. All mechanical motions are controlled by stepper drivers and embedded microcontrollers. The entire setup is controlled by a custom MATLAB graphical user interface (GUI), shown in Figure 4b.

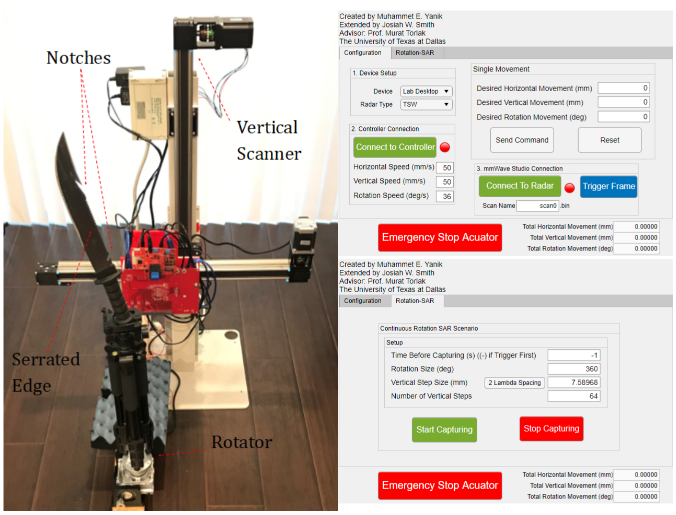

(a) Custom Prototype Scanner (b) MATLAB GUI

Fig. 4: Rotation-ISAR Scanner and MATLAB GUI

VIII. Imaging Results

The 2-D vertical and rotational scan is performed by the prototype scanner. The large knife shown in Figure 4a is mounted to the rotator at an angle and scanned. Note the knife's notches and serrated edge. First, a scan is conducted using only a single channel and

A. SISO Imaging Results

In the first experiment, a single transceiver pair is used to simulate a full-duplex SISO transceiver. Since the MIMO virtual array consists of 8 equally spaced virtual elements spanning 2λ, the SISO scan will have a vertical spacing of $\lambda/4$ and will require 512 vertical captures to replicate the MIMO scan. All other parameters will remain the same, as shown in table II.

TABLE II: SISO Radar Parameters

R_0	$\Delta\theta$	θ_{max}	N_y	Δy	B	f_c
0.25 m	0.036°	360°	512	$\lambda/4$	4 GHz	79 GHz

Once the scan is complete, the proposed MIMO R-ISAR 3-D holographic imaging algorithm is computed to reconstruct the 3-D target. 3-D volume rendering and maximum intensity profile (MIP) images are shown in Figure 5. As expected, the knife is easily visible, along with its notches and serrated edge. The entire scan took nearly two and a half hours to complete. By exploiting the nature of the MIMO virtual array, this scanning time can be drastically reduced. The algorithm proposed in Section IV allows for this drastic reduction in scanning time without increasing the computational complexity of the image reconstruction algorithm.

we may not need different visualizations.

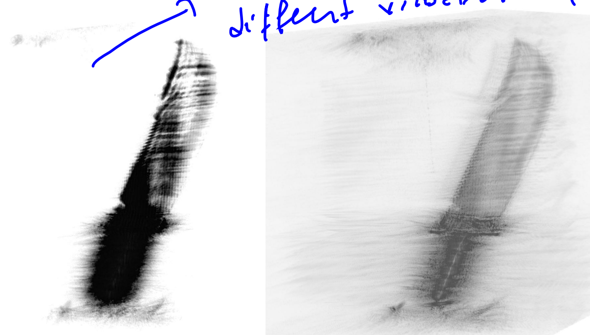

(a) Volume Rendering (b) Maximum Intensity Profile

Fig. 5: SISO Reconstructed Image of Knife

instead, let's put some more real-life applications

B. MIMO Imaging Results

Now, the knife is scanned again, this time using all 2 Tx and 4 Tx antennas on the TI IWR1443-Boost. Before the multistatic-to-monostatic conversion and subsequent image reconstruction algorithm, the array calibration technique described in [16] is employed to calibrate the phase of the echo signal and mitigate instrument delay. Then, the calibrated echo data is processed by the proposed R-ISAR MIMO 3-D holographic imaging algorithm and a high-resolution 3-D image is produced. Again, 3-D renderings are included below, in Figure 6. The MIMO scan only took less than twenty minutes to complete, a significant reduction in comparison to the SISO scan.

Examining both the SISO and MIMO images qualitatively, the image quality of the MIMO image appears to be the same, if not better, than that of the SISO scan. In fact, some artifacts at the top of the knife blade are visible in the horizontal domain of the SISO MIP image that are not visible in the MIMO image. This is likely do to a minor misalignment error

(a) Volume Rendering

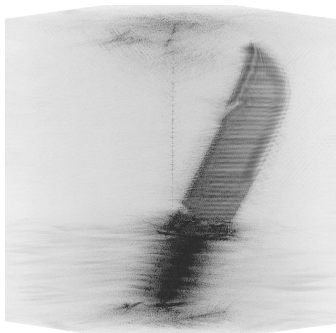

(b) Maximum Intensity Profile

Fig. 6: MIMO Reconstructed Image of Knife

in the rotational scan due to the large number of scans required for the SISO scan. These artifacts are likely not found in the MIMO scan since an eighth of the scans are required. By using the algorithm proposed in this paper, we were able to drastically reduce the scanning time while maintaining the computational efficiency of the SISO-based algorithms.

IX. Conclusion

In this paper, we derived an efficient MIMO rotational-ISAR 3-D holographic imaging algorithm based on the single pixel polar formatting algorithm and multistatic-to-monostatic conversion. The algorithm successfully pairs the scanning efficiency of MIMO systems with the computational efficiency of SISO reconstruction algorithms. Additionally, we developed a complete, robust 3-D imaging system consisting of a vertically scanned MIMO radar and a rotator to rotate the target object. Our system fully integrates scanning scenario setup, data collection and calibration, algorithm implementation, and image inspection for a complete, efficient 3-D holographic imaging platform. Using this prototype system, high-resolution images are captured to demonstrated the effectiveness of this system for 3-D scene reconstruction and verify the MIMO R-ISAR algorithm's performance in comparison to its SISO counterpart. The algorithm and system demonstrate high-performance near-field imaging using MIMO rotational inverse synthetic radar radar.

Acknowledgment

This work is supported by Semiconductor Research Corporation (SRC) task 2712.029 through The University of Texas at Dallas' Texas Analog Center of Excellence (TxACE).

References

[1] D. M. Sheen, J. L. Fernandes, J. R. Tedeschi, D. L. McMakin, A. M. Jones, W. M. Lechelt, and R. H. Severtsen, "Wide-bandwidth, wide-beamwidth, high-resolution, millimeter-wave imaging for concealed weapon detection," in *Passive and Active Millimeter-Wave Imaging XVI*, D. A. Wikner and A. R. Luukanen, Eds., vol. 8715, International Society for Optics and Photonics. SPIE, 2013, pp. 65 – 75. [Online]. Available: https://doi.org/10.1117/12.2016132

[2] X. Zhuge and A. G. Yarovoy, "A sparse aperture mimo-sar-based uwb imaging system for concealed weapon detection," *IEEE Transactions on Geoscience and Remote Sensing*, vol. 49, no. 1, pp. 509–518, 2011.

[3] M. E. Yanik and M. Torlak, "Near-field 2-D SAR imaging by millimeter-wave radar for concealed item detection," in *Proc. IEEE Radio and Wireless Symp.*, Orlando, FL, USA, Jan. 2019, pp. 1–4.

[4] X. Zhuge, A. G. Yarovoy, T. Savelyev, and L. Ligthart, "Modified kirchhoff migration for uwb mimo array-based radar imaging," *IEEE Transactions on Geoscience and Remote Sensing*, vol. 48, no. 6, pp. 2692–2703, 2010.

[5] B. Baccouche, P. Agostini, S. Mohammadzadeh, M. Kahl, C. Weisenstein, J. Jonuscheit, A. Keil, T. Löffler, W. Sauer-Greff, R. Urbansky, P. H. Bolívar, and F. Friederich, "Three-dimensional terahertz imaging with sparse multistatic line arrays," *IEEE Journal of Selected Topics in Quantum Electronics*, vol. 23, no. 4, pp. 1–11, 2017.

[6] H. Liu, Y. X. Zhang, Z. J. Long, F. Han, and Q. H. Liu, "Three-dimensional reverse-time migration applied to a mimo gpr system for subsurface imaging," in *2016 16th International Conference on Ground Penetrating Radar (GPR)*, 2016, pp. 1–4.

[7] M. E. Yanik and M. Torlak, "Millimeter-wave near-field imaging with two-dimensional SAR data," in *Proc. SRC Techcon*, no. P093929, Austin, TX, USA, Sep. 2018.

[8] L. Qiao, Y. Wang, Z. Shen, Z. Zhao, and Z. Chen, "Compressive sensing for direct millimeter-wave holographic imaging," *Appl. Opt.*, vol. 54, no. 11, pp. 3280–3289, Apr 2015. [Online]. Available: http://ao.osa.org/abstract.cfm?URI=ao-54-11-3280

[9] D. M. Sheen, D. L. McMakin, and T. E. Hall, "Near-field three-dimensional radar imaging techniques and applications," *Appl. Opt.*, vol. 49, no. 19, pp. E83–E93, Jul. 2010.

[10] Sheen, McMakin, and Hall, "Three-dimensional millimeter-wave imaging for concealed weapon detection," *IEEE Trans. on Microwave Theory and Techniques*, vol. 49, no. 9, pp. 1581–1592, Sep. 2001.

[11] X. Zhuge and A. G. Yarovoy, "Three-dimensional near-field mimo array imaging using range migration techniques," *IEEE Transactions on Image Processing*, vol. 21, no. 6, pp. 3026–3033, 2012.

[12] J. Gao, B. Deng, Y. Qin, H. Wang, and X. Li, "Efficient terahertz wide-angle nufft-based inverse synthetic aperture imaging considering spherical wavefront," *Sensors (Basel, Switzerland)*, vol. 16, no. 12, p. 2120, Dec 2016, 27983618[pmid]. [Online]. Available: https://pubmed.ncbi.nlm.nih.gov/27983618

[13] J. Gao, B. Deng, Y. Qin, H. Wang, and X. Li, "An efficient algorithm for mimo cylindrical millimeter-wave holographic 3-d imaging," *IEEE Transactions on Microwave Theory and Techniques*, vol. 66, no. 11, pp. 5065–5074, 2018.

[14] D. M. Sheen, D. L. McMakin, T. E. Hall, and R. H. Severtsen, "Real-time wideband cylindrical holographic surveillance system."

[15] J. Laviada, A. Arboleya-Arboleya, Y. Álvarez, B. González-Valdés, and F. Las-Heras, "Multiview three-dimensional reconstruction by millimetre-wave portable camera," *Scientific reports*, vol. 7, no. 1, pp. 6479–6479, Jul 2017, 28743908[pmid]. [Online]. Available: https://pubmed.ncbi.nlm.nih.gov/28743908

[16] M. E. Yanik and M. Torlak, "Near-field MIMO-SAR millimeter-wave imaging with sparsely sampled aperture data," *IEEE Access*, vol. 7, pp. 31 801–31 819, Mar. 2019.

[17] M. E. Yanik, D. Wang, and M. Torlak, "3-d mimo-sar imaging using multi-chip cascaded millimeter-wave sensors," in *2019 IEEE Global Conference on Signal and Information Processing (GlobalSIP)*, 2019, pp. 1–5.

[18] J. Detlefsen, A. Dallinger, S. Huber, and S. Schelkshorn, "Effective reconstruction approaches to millimeter-wave imaging of humans," 01 2005.

[19] D. G. Dudley, *Electromagnetic Sources*, 1994, pp. 139–180.

[20] T. Vaupel and T. F. Eibert, "Comparison and application of near-field isar imaging techniques for far-field radar cross section determination," *IEEE Transactions on Antennas and Propagation*, vol. 54, no. 1, pp. 144–151, 2006.

[21] J. K. Gao, Y. L. Qin, B. Deng, H. Q. Wang, J. Li, and X. Li, "Terahertz wide-angle imaging and analysis on plane-wave criteria based on inverse synthetic aperture techniques," *Journal of Infrared, Millimeter, and Terahertz Waves*, vol. 37, no. 4, pp. 373–393, 2016. [Online]. Available: https://doi.org/10.1007/s10762-016-0249-x

[22] A. Ishimaru, Tsz-King Chan, and Y. Kuga, "An imaging technique using confocal circular synthetic aperture radar," *IEEE Transactions on Geoscience and Remote Sensing*, vol. 36, no. 5, pp. 1524–1530, 1998.

[23] Texas Instruments mmWave sensors. [Online]. Available: http://www.ti.com/sensors/mmwave/overview.html